Narrowband emission line imaging spectrometry using Savart plates

Bryan Maione[a]*, Leandra Brickson[a], Michael Kudenov[a], Michael Escuti[a]
[a]North Carolina State University, Department of Electrical and Computer Engineering, Raleigh, NC

Abstract

Polarization spatial heterodyne interferometry (PSHI) allows for the development of compact, vibration insensitive, high spectral resolution sensors. Introducing the imaging qualities of a lenslet array extends the advantages of PSHI to imaging interferometers. The use of Savart plates enables a birefringent interferometer that obtains higher spectral resolution with fewer optical aberrations when compared to alternative designs. In this paper, we describe the design, construction, calibration and validation of a narrowband emission line imaging spectrometer (NELIS), based on Savart plates and liquid crystal polarization gratings, along with its associated theoretical model. This sensor is advantageous for spectral imaging in the areas of remote sensing, biomedical imaging and machine vision.

1.0 Introduction

High spectral resolution, narrow band spectral imaging has found applications in Fraunhofer line discrimination (FLD) and biomedical sensing. Realizing these systems using common-path interferometry and snapshot imaging creates a class of sensors fit for remote sensing. Vibration insensitivity, characteristic of common-path interferometry, is ideal for ground and airborne platforms. Utilizing Savart plates maintains the common-path advantage while additionally supplying nanometer scale spectral resolutions. Additionally, the use of liquid crystal polarization gratings enables sampling advantages characteristic of spatial heterodyning [1]. The division of aperture approach of snapshot imaging enables a full spectral acquisition with each frame of raw data.

In this work a narrowband emission line imaging spectrometer (NELIS) is described. The NELIS is a narrow band high resolution spectral imager based on polarization elements and refractive optics. A linearly varying optical path difference (OPD) is obtained using Savart plates and the resulting interference is measured using a FPA. Additionally, a 5x5 lenslet array is used and has its foci relayed to the interference localization plane on the FPA. This results in a 5x5 repetition of the scene with interference fringes superimposed upon them. From this a three dimensional data cube can be constructed where X and Y correspond to the traditional spatial dimensions while Z corresponds to OPD. Using Fourier optics techniques, the OPD dimension can be transformed to obtain spectral content. In section 2 we detail the design and operation of the NELIS from a polarization ray trace and interference perspective. Section 3 outlines experiments and setups for aligning and bonding the Savart plate components. Section 4 describes the spectral calibration approach. Lastly, section 5 presents the operation of the sensor in an outdoor scene.

2.0 Theory

Snapshot spectral imaging enables a full spatial and spectral acquisition with each frame of data. The raw MxN repetitions of the scene are registered using static image registration coefficients, which are calculated beforehand. Registering each sub-image creates a 3D data array corresponding to *x, y* and optical path difference (OPD). Using Fourier optical techniques the non-

*bdmaione@ncsu.edu

Polarization: Measurement, Analysis, and Remote Sensing XII, edited by David B. Chenault, Dennis H. Goldstein,
Proc. of SPIE Vol. 9853, 985309 · © 2016 SPIE · CCC code: 0277-786X/16/$18 · doi: 10.1117/12.2224275

calibrated registered data array can be transformed to a calibrated spectral image. Fig. 1 depicts the snapshot methodology as developed in past work [2].

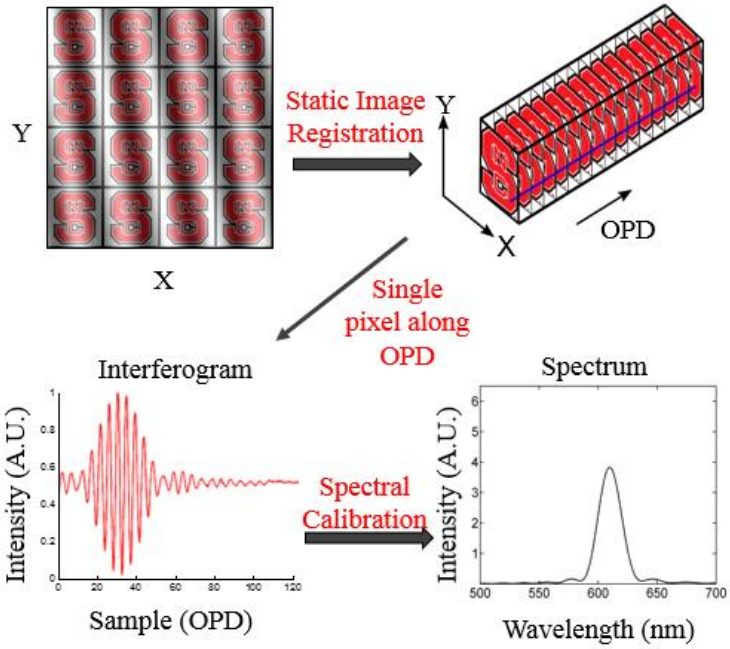

Fig. 1 Snapshot spectral imaging methodology and processing steps.

2.1 Savart plate interferometer

The NELIS is a snapshot spectral imager based on a Savart plate interferometer and spatial heterodyning polarization gratings (PGs). A Savart plate interferometer can be modeled nearly identically to Young's double pinhole interferometer (YDPI). A Savart plate consists of two beam displacers (BDs), with fast axes at 45 degrees and 135 degrees in the *yz* plane, as illustrated below in Fig. 2. These two sheared beams are then incident onto an imaging lens before converging onto a focal plane array (FPA). Additionally, field widening of the interference is enabled with the use of a half wave plate, which is placed in beween the two beam displacers as shown.

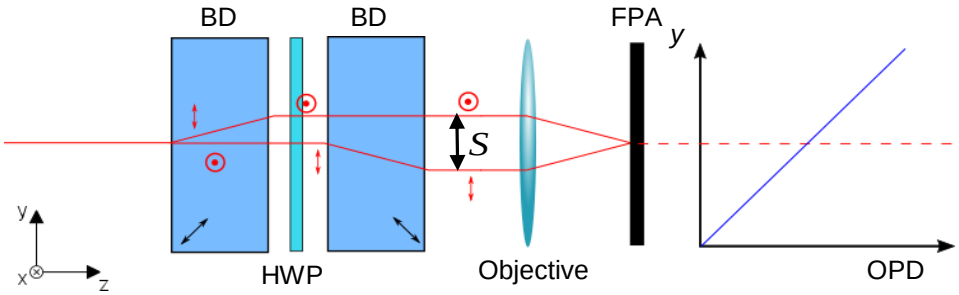

Fig. 2 Savart plate interferometer beam path and OPD spatial dependence.

Unlike a YDPI, a Savart plate generates interference by interfering orthogonal linear polarization states. A shear, *S*, is produced between the orthogonal states. It can be shown that the shear imparted by a Savart plate can be described as,

$$S = 2t\frac{a^2 - b^2}{a^2 + b^2}, \tag{1}$$

where t is the thickness of the beam displacers, $a = 1/n_e$ and $b = 1/n_o$, and n_o and n_e are the ordinary and extraordinary indices of refraction for the beam displacer material [3]. Shear in a Savart plate is analogous to the pinhole spacing in a YDPI, as it is responsible for the maximum OPD and subsequently the spectral resolution of the system. Fig. 2 depicts a polarization ray trace through a Savart plate interferometer. Using the methodology and geometry from a YDPI, the interference pattern associated with a Savart plate interferometer can be calculated as

$$I = \cos\left(\frac{2\pi}{\lambda}\frac{yS}{f}\right) \tag{2}$$

where λ is the wavelength of the incident light, y is the location on the FPA, and f is the focal length of the objective lens.

2.2 Polarization grating interferometer

A similar setup can be used to characterize the influence of the polarization gratings. While spatial heterodying using PGs is well documented in past work, they have not been used to compensate a Savart plate as they are in this system [4]. Polarization gratings are a liquid crystal based device that leverages geometric (Pancharatnam-Berry) phase [5]. For a linearly polarized input a single PG outputs +/- 1 orders that are right and left circularly polarized. In this work we utilize PGs for their high diffraction efficiency (>99%) in to the +/- 1 orders. Fig. 3 depicts a ray trace through a polarization grating (PG) based interferometer.

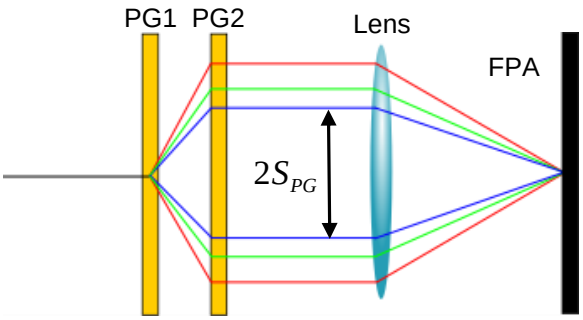

Fig. 3 Ray trace through a polarization grating interferometer.

This simple setup consists of two stacked polarization gratings separated by a thickness t and a fringe localization lens, with focal length f. The lens collects the beams which allows them to interfere on the FPA. Interference due to stacked PGs and a lens is of the form,

$$I = \cos\left(\frac{4\pi ty}{\Lambda f}\right) \tag{3}$$

where Λ is the period of the grating and f is the focal length of the lens. Due to the diffractive nature of the PGs, their interference does not depend on wavelength. This makes the polarization gratings ideal for introducing a wavelength-independent spatial frequency offset in the optical path difference (*i.e.*, spatial heterodyning) of a birefringent interferometer

2.3 Imaging polarization heterodyned interferometer

Combining a Savart plate interferometer with polarization gratings is the fundamental basis for the NELIS. The NELIS consists of a calcite Savart plate, two sets of stacked polarization gratings, a 5x5 lenslet array and commercial off-the-shelf Nikon collimating and reimaging lenses.

In this system, foreoptics (not shown) are used to relay collimated object light into the lenslet array. Fig. 4 depicts a ray trace through the system where the diffractive (PG) and refrative (SP) influence occurs simultaneously.

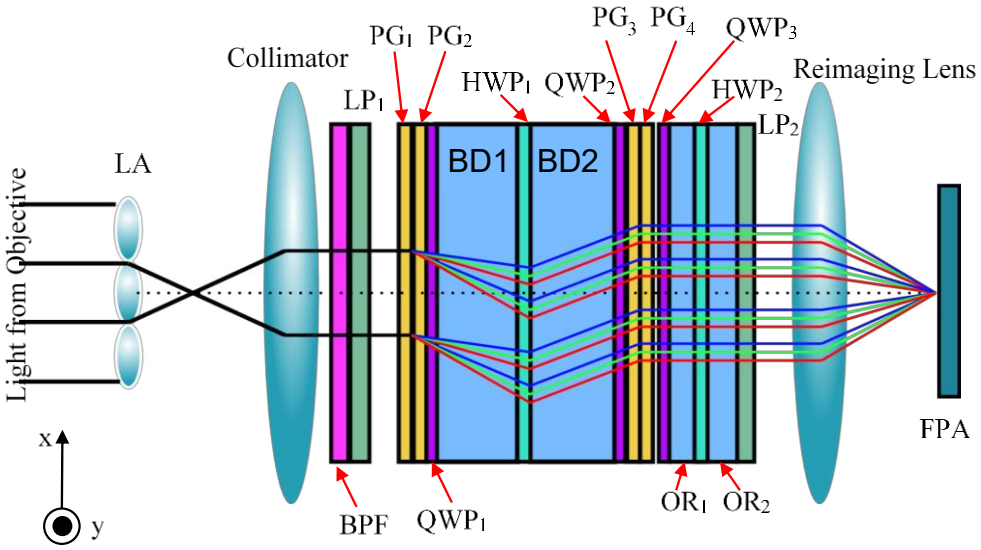

Fig. 4 Ray trace through the components of the NELIS system.

Light from the 5×5 lenslet array (LA) is collected and collimated by a Nikon F/1.2 collimating lens and subsequently filtered by a spectral band pass filter (BPF). The collimated ray bundle is incident on a linear polarizer LP1, oriented with a transmission axis at 45 degrees. Transmitted light is then incident on the first PG grouping, created by gratings PG_1 and PG_2. These gratings diffract the linear states into equal amplitude right and left circular polarizations. Using two groups of PGs introduces an additional degree of freedom to tune the heterodyne wavelength of the system by counter roatating their grating vectors. The heterodyne wavelength is the new zero spatial frequency wavelength for the system and can be described as

$$\lambda_h = \frac{\Lambda BS}{f}, \tag{4}$$

where B is the birefringence of the Savart plate material and is defined as $B=(n_e-n_o)$ [4]. The first quarter wave plate (QWP1) converts the right hand circular (RHC) and left hand circular (LHC) polarizations back to linear 45 and 135 degrees respectively. Each linear state is refracted by the first beam displacer and converted to the orthogonal linear state with the half wave plate. HWP_1 provides field widening for the system [6]. After the polarization states are converted, they are again refracted by the second beam displacer. The collective effect of the two beam displacers and the HWP is a shear between the orthogonal polarization states. Each sheared state is then converted to RHC and LHC polarization with QWP_2 and then rediffracted by PG3 and PG4. Without QWP_2, each linear state would not couple directly into the polarization grating's eigenstates, resulting in 4 beams rather than 2. Lastly, QWP_3 converts the circularly polarized beams to their orthogonal linear states to interact with the field widened offset retarder (OR) which is a combination of OR_1, OR_2 and HWP_2. Finally the sheared beams are collected by the Nikon reimaging lens to produce a focus on the FPA for all the sub-images that is coincident with the fringe localization plane. This process creates the raw data frames as shown in Fig. 1. The

interference fringes generated by this system has contributions from both the Savart plate and the polarization gratings and are modeled as

$$I = \cos\left(\frac{2\pi}{\lambda}\left(\frac{yS}{f} - \frac{2\lambda ty}{\Lambda f}\right)\right). \tag{5}$$

From this it is clear that the polarization gratings introduce a static subtractive offset in frequency from the Savart plate system alone. This capability reduces the spatial frequency of the fringes seen by the FPA.

3.0 Bonding and system alignment

3.1 Bonding of calcite components

A custom setup for bonding the Savart plate elements and the polymer waveplates is shown in Fig. 5. The setup consists of a generating and analyzing polarizer, a customized rotation mount with lock pins, an unpolarized HeNe laser and a CCD. The CCD is interfaced to the Matlab image acquisition (IMAQ) toolbox. Utilizing the IMAQ toolbox enables real time region of interest (ROI) monitoring. Doing so enables tracking of power in sheared beams.

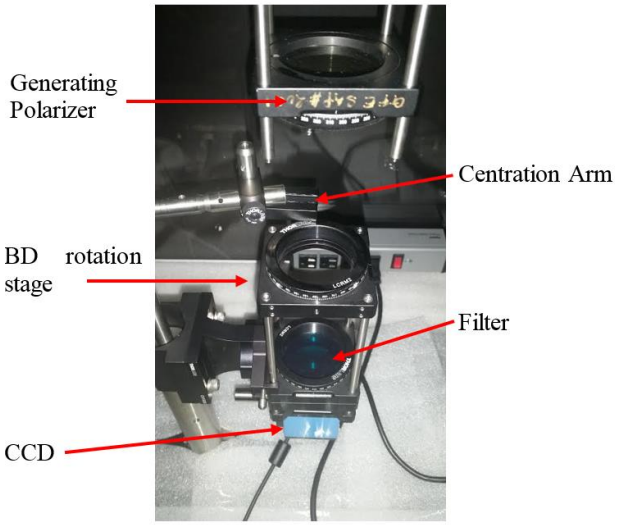

Fig. 5 Alignment setup for the bonding of calcite components utilizing an imaging source USB camera.

By tracking the power in the sheared beams of the Savart plate it was possible to precicely align the two beam displacer elements with a half wave plate. Proper alignment is reached when rotation of the half wave plate between the two beam displacers results in two equally powered beams in the upper and lower ROI as shown in Fig. 6.

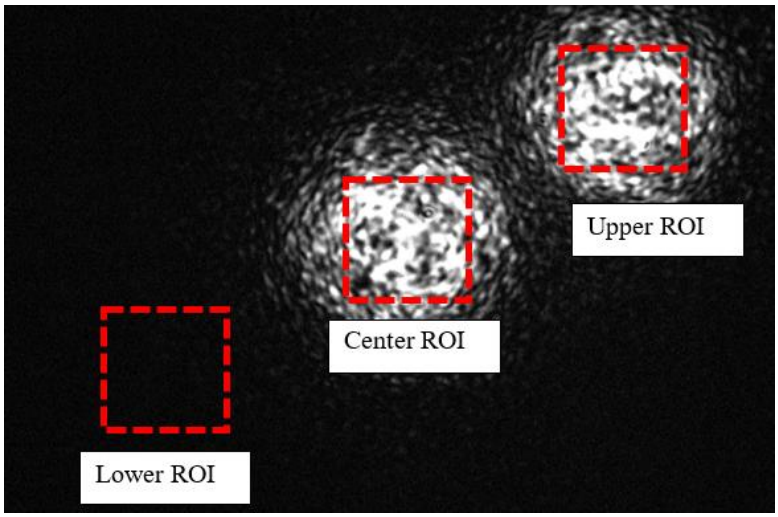

Fig. 6. Snapshot of the Matlab image acquisition interface with marked regions of interest.

The mean value of each ROI was monitored in real time while rotating the elements. Once equal power in the EO and OE beams of the Savart plate were achieved the grouping was bonded with NOA 61 adhesive and cured under a Bond wand.

The quarter wave plates on each of the Savart plate were aligned by first rotating the generating polarizer to a null in either the EO, or OE (upper and lower ROI respectively) beam. Each QWP was then rotated such that the intensity in the previously null ROI is maximized.

3.2 System Alignment

Following bonding of calcite components, the system has been assembled and aligned in the optomechanical mounts. Each grouping was affixed to its rotation mount using Silicone RTV and Kapton tape. Once inserted in to their respective mounts each element was aligned precisely to its nominal orientation (as determined in simulation) with respect to the shearing axis of the Savart plate. Following nominal orientation of each element the assembly was placed in the optomechanical stepup shown in Fig. 7. Once assembled final adjustments were made by modifying the orientation of the polarization gratings. Doing so enabled fine adjustment in the orientation and contrast of the interference fringes generated by the system.

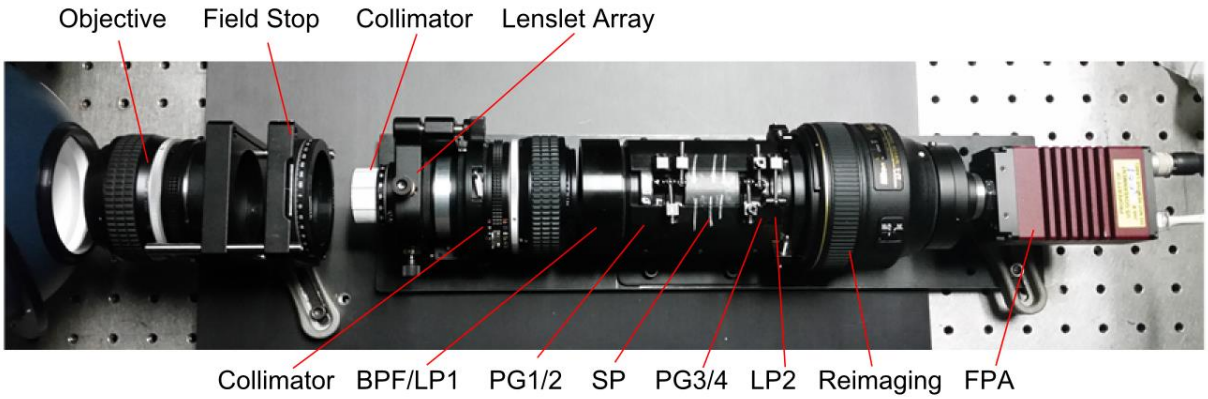

Fig. 7 Assembled and aligned Savart plate interferometer with fore optic.

4.0 Spectral Calibration

The first step in the calibration procedure is to calculate image registration coefficients using an image registration target; this processes is shown in the first step of Fig. 1. Note: this process only needs to be performed one time for a given system alignment.

In this process, two out of phase images of the image registration target are added together to produce a fringeless image. The user then specifies the sub-image size and the coordinates for the center sub-image. For this alignment, each sub-image is 500 by 380 pixels. This image will be used as the master image for the image registration.

Once the master image has been extracted, it is auto correlated with the fringeless image registration target image to determine the centroids of each sub-image. Each sub-image is then extracted and stacked to produce an unregistered data cube, which is then registered to the master image using an optic flow-based image registration algorithm. The algorithm ensures that every corresponding pixel in each sub-image is associated with the same object point on the image registration target. Following the optic flow algorithm, the registered centroids of each sub-image are saved and can be applied to any raw image acquired using the interferometer.

4.1 Linear unmixing algorithm

Once image registration coefficients have been calculated they can be saved and applied to any image acquired by the SHIFT as long as the alignment does not change. Initially the coefficients are applied to a Tungsten and Potassium basis image after being divided by a fringeless flat field image. Both basis images are collected by aiming a High Pressure Sodium (HPS) source and a Tungsten-Halogen source in to an integrating sphere. Due to the narrow band nature of the sensor 760 nm - 780 nm these two basis images are adequate. For a given alignment once these two calibration images have been acquired linear unmixing can be performed on any scene image.

The linear unmixing algorithm is founded on linear combination analysis. Meaning each interferogram contained at each pixel in the scene image can be represented as a linear combination of the basis interferograms. This is best described using the linear equation

$$\mathbf{I} = \mathbf{AS} \tag{6}$$

In equation (6) **S** is a matrix containing the basis interferograms extracted from a single pixel of the two registered K and W basis images. **I** is the scene interferogram extracted from the registered scene image. In order for the unmixing to work properly it is important that the interferogram extracted from the scene and basis images correspond to the same pixel in the registered images. In this instance two basis interferograms are used, thus **S** is the size Nx2 where N is the number of lenslets in the system (N = 25). The goal of the unmixing procedure is to determine the relative mixing of the basis interferograms in the scene interferogram. Assume that **A** is an "abundance" vector, which contains the multiplicative coefficients for linear combination. Since **S** contains two basis interferograms, equation (6) reduces to

$$\mathbf{I} = a_W S_W + a_K S_K, \tag{7}$$

where a_W and a_K are the abundance values for the Tungsten and Potassium basis interferograms respectively. An abundance value of zero implies that the scene interferogram contains no component of that particular basis. The matrix pseudo inversion in equation (8) is used to

determine the values of a_W and a_K that correspond to the pixel associated with the scene interferogram.

$$[a_W, a_K] = \mathbf{S}^{-1}\mathbf{I} \tag{8}$$

This process is repeated for each pixel and associated interferogram in the scene interferogram cube. The collective abundance values for all pixels in the interferogram cube are used to construct two abundance images. One abundance image corresponds to the Potassium abundance and the other corresponds to the Tungsten abundance.

5.0 Results

In order to further test the utility of the sensor and linear unmixing calibration, an outdoor scene was constructed using Estes solid model rocket engines, which contain potassium nitrate, and a Tungsten lamp. Prior to imaging an engine using the NELIS, a plume was first measured using an Ocean Optics spectrometer to determine if the rocket possessed the potassium emission lines. The result of this test is shown in Fig. 8 and it is clear that it resembles the spectra from the HPS lamp.

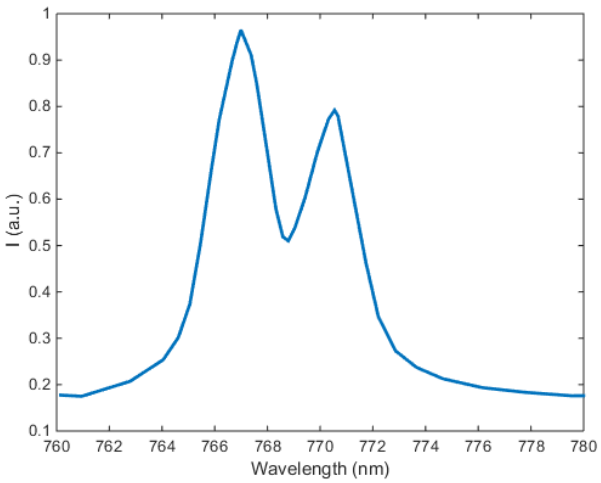

Fig. 8 Potassium emission lines from a model rocket engine obtained with a fiber and an Ocean Optics spectrometer.

After verifying the model rocket engines possess the emission spectrum of interest, a scene was constructed by igniting a model rocket engine and acquiring frames with the NELIS. In order to mimic a sun glint, the Tungsten lamp was aimed directly into the sensor. Fig. 9 (a) shows the outdoor scene setup with an ignited rocket obtained using a digital camera while Fig. 9 (b) shows the band integrated image from the NELIS.

(a) (b)

Fig. 9 Scene with model rocket engine and Tungsten lamp obtained with a camera and the NELIS.

One of the most significant features of these two images is that the Tungsten lamp appears brighter in the color image. However, within the band pass of interest, the rocket engine is noticeably brighter due to the strong Potassium emission lines. After applying the image registration coefficients the linear unmixing algorithm was applied and the abundance images were constructed. The background and potassium abundance images are shown in Fig. 10.

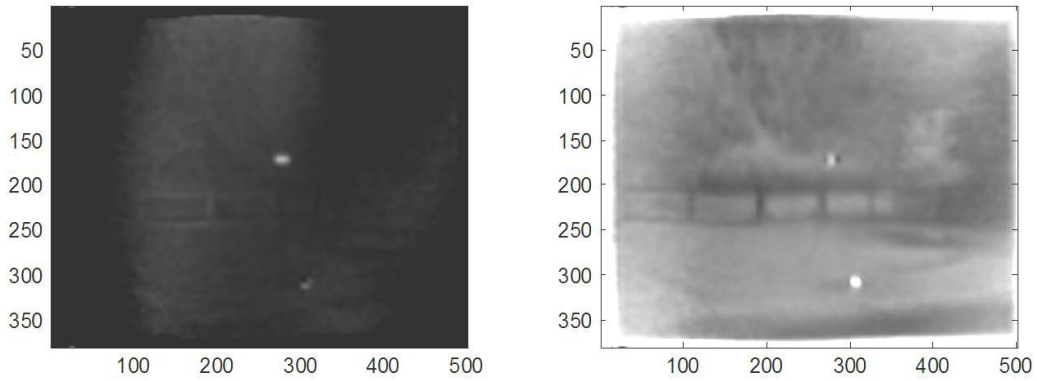

Fig. 10 (Left) Potassium and (right) Background abundance images from linear unmixing for frame 63 of a rocket ignition video sequence.

The linear unmixing algorithm is fairly robust in the presence of near point sources and sun glints; however, it does allow for some cross-talk between the potassium and background spectra. For instance, in the potassium image, the tungsten lamp does possess a small signal. However, the rocket engine is a factor of 2 brighter; thus, a simple threshold operation would be adequate to distinguish the two signals in a real scenario. For further verification of the unmixing process in the presence of a weaker Potassium signature, another experiment was performed by dissolving potassium salt in water and spraying it in to a propane torch. Fig. 11 shows the results of the linear unmixing for this scene.

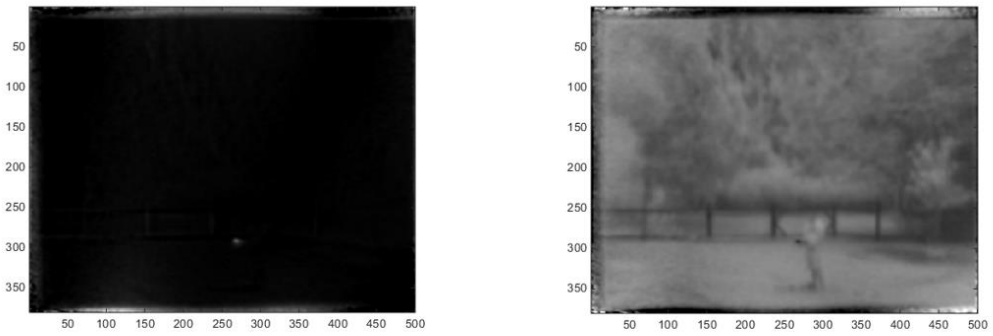

Fig. 11 Potassium salt sprayed into a propane torch. (a) Potassium and (b) background abundance images.

In the case of the linear unmixing algorithm, there is some cross-talk between the background spectra and the potassium spectra in that some color is evident within regions containing only background. This type of behavior is more evident in Fig. 12 below, which represents some selected frames from the video data. Notable is the red background, indicating the 'detection' of potassium where no potassium is present.

Fig. 12 Select frames from the video sequence, illustrating remaining crosstalk between the background and potassium signatures.

6.0 **Conclusions**

Modeling, alignment and testing of a narrowband emission line spectral imaging sensor has been demonstrated. The use of a linear unmixing procedure has proven adequate in the discrimination of Potassium emission lines from sun glints. However, in the unmixing procedure some crosstalk exists between the emission line and background channels.

Future work in the use of the NELIS sensor will address the utilizations of different calibration procedures to reduce or eliminate crosstalk between the spectral channels. Particularly the device will be calibrated using a neural network trained with monochromatic H-matrix data.

7.0 **Acknowledgements**

This work was supported by the Air Force Research Laboratory (AFRL), United States Air Force, under Contract Number: FA8650-13-C-1589. NCSU acknowledges support from SA Photonics Inc. Released by AFRL/RYMT for public distribution, <3/3/16>, v1.
Additionally, LB and ME acknowledge the partial support of the National Science Foundation (CAREER award ECCS-0955127) in this work.

8.0 References

[1] J. M. Harlander, F. L. Roesler, J. G. Cardon, C. R. Englert, and R. R. Conway, "SHIMMER: a spatial heterodyne spectrometer for remote sensing of earth's middle atmosphere," *Appl. Opt.*, vol. 41, no. 7, pp. 1343–1352, Mar. 2002.

[2] M. W. Kudenov and E. L. Dereniak, "Compact real-time birefringent imaging spectrometer," *Opt. Express*, vol. 20, no. 16, pp. 17973–17986, Jul. 2012.

[3] D. Malacara, *Optical Shop Testing*. John Wiley & Sons, 2007.

[4] M. W. Kudenov, M. N. Miskiewicz, M. J. Escuti, and E. L. Dereniak, "Spatial heterodyne interferometry with polarization gratings," *Opt. Lett.*, vol. 37, no. 21, pp. 4413–4415, Nov. 2012.

[5] J. Kim, Y. Li, M. N. Miskiewicz, C. Oh, M. W. Kudenov, and M. J. Escuti, "Fabrication of ideal geometric-phase holograms with arbitrary wavefronts," *Optica*, vol. 2, no. 11, p. 958,

[6] M. Françon, "Polarization Apparatus for Interference Microscopy and Macroscopy of Isotropic Transparent Objects*," *J. Opt. Soc. Am.*, vol. 47, no. 6, p. 528, Jun. 1957.
Nov. 2015.